





Article

Validation of a CFD-Based Numerical Wave Tank Model of the 1/20th Scale Wavestar Wave Energy Converter

Christian Windt ^{1,*} , Nicolás Faedo ¹ , Demián García-Violini ² , Yerai Peña-Sanchez ¹ ,
Josh Davidson ³ , Francesco Ferri ⁴  and John V. Ringwood ¹ 

- ¹ Centre for Ocean Energy Research, Maynooth University, W23 F2H6 Co. Kildare, Ireland; nicolas.faedo.2017@mumail.ie (N.F.); yerai.pena.2017@mumail.ie (Y.P.-S.); John.Ringwood@mu.ie (J.V.R.)
 - ² Departamento de Ciencia y Tecnología, Universidad Nacional de Quilmes, Buenos Aires B1876, Argentina; ddgv83@gmail.com
 - ³ Department of Fluid Mechanics, Faculty of Mechanical Engineering, Budapest University of Technology and Economics, H-1111 Budapest, Hungary; davidson@ara.bme.hu
 - ⁴ Department of Civil Engineering, Faculty of Engineering and Science, Aalborg University, 9220 Aalborg, Denmark; ff@civil.aau.dk
- * Correspondence: christian.windt.2017@mumail.ie

Received: 12 June 2020; Accepted: 11 July 2020; Published: 14 July 2020



Abstract: Numerical wave tanks (NWTs) provide efficient test beds for the numerical analysis at various stages during the development of wave energy converters (WECs). To ensure the acquisition of accurate, high-fidelity data sets, validation of NWTs is a crucial step. However, using experimental data as reference during model validation, exact knowledge of all system parameters is required, which may not always be available, thus making an incremental validation inevitable. The present paper documents the numerical model validation of a 1/20 scale Wavestar WEC. The validation is performed considering different test case of increasing complexity: wave-only, wave excitation force, free decay, forced oscillation, and wave-induced motion cases. The results show acceptable agreement between the numerical and experimental data so that, under the well-known modelling constraints for mechanical friction and uncertainties in the physical model properties, the developed numerical model can be declared as validated.

Keywords: model validation; numerical wave tank; CFD; OpenFOAM; wave-structure interaction

1. Introduction

The numerical modelling of the wave-structure interaction (WSI) is an integral part of the development of wave energy converters (WECs), complementing physical wave tank tests. Compared to physical wave tanks, numerical wave tanks (NWTs) provide an excellent numerical tool, allowing the investigation of different WEC designs and scales, with the ability to passively measure relevant variables at arbitrary locations throughout the NWT. In particular, computational fluid dynamics (CFD)-based NWTs can provide high-fidelity data sets to support the WEC development.

To ensure high-fidelity of the generated data, CFD-based NWTs rely on both verification and validation [1]. Verification embraces the quantification of spatial and temporal discretisation errors using convergence studies. Validation covers the comparison of numerical results to reference data. In general, four different validation strategies can be identified, in which CFD results are compared to:

- Analytical results
- Low- to mid-fidelity numerical data

- Third-party CFD-based NWT data
- Experimental data

In the comprehensive review of CFD-based NWTs for WEC applications in [2], experimental data has been identified as the most common reference during model validation, which is typically only available from scale model testing in physical wave tanks.

1.1. Related Studies

Dai et al. [3] validate a numerical model of a fixed oscillating water column, against physical wave tank tests, to analyse scale effects. Two different scales (with a scale ratio of 1:3) are considered in both an experimental and numerical test frameworks. For the experimental measurement uncertainty, the authors follow the recommendations in [4]. Comparing the response amplitude operators (RAOs) and the captured power between experimental and numerical results, discrepancies of up to 15% are observed when including measurement uncertainty.

Xu et al. [5] perform experimental and numerical analysis of a two-body, floating point-absorber type WEC, in operational and survival conditions. For both conditions, independent experimental test campaigns, in different test facilities and at different scales, were performed. For the survivability test cases, discrepancies for the surge and pitch RAOs are attributed to a mismatch in the model geometries and the centre of mass (CoM).

Windt et al. [6] validate a 1/5th scale NWT model of the Wavestar WEC, for power production assessment, finding discrepancies between physical and numerical results for the surface elevation, body motion, pressure on the hull, and power take-off force, of the order of $\mathcal{O}(10\%)$. It is highlighted that the validation of complex physical systems requires exact knowledge of all system characteristics for the formulation of assumptions in the numerical model. This detailed knowledge is difficult to acquire and inaccuracies may influence the achievable order of accuracy for validation studies.

Ransley et al. [7,8] present the results of the Blind Test Series 2 and 3, organised by the Collaborative Computational Project in WSI (CCP-WSI), considering two moored, floating point absorber type WECs, exposed to focused waves. The authors perform comprehensive code-to-experiments and code-to-code comparisons, highlighting, amongst others, the importance of an accurate representation of the incident wave for a successful replication of the wave-driven WEC motion within the NWT.

1.2. Objectives

Validating a CFD-based NWT model against experimental data risks the danger of drawing false conclusions if not all crucial system parameters are available with a high precision and/or the system under investigation is too complex. Thus, when using experimental data as the reference, an incremental validation procedure is recommended, considering different test cases of increasing complexity, to identify error propagation between the cases and ensure the fidelity of the CFD-based NWT.

Recently, a set of experimental tank tests of a 1/20th scale Wavestar model were conducted at Aalborg University, as part of the International WEC Control Competition (WECCOMP) [9]. This paper aims at the validation of a CFD-based NWT model of the 1/20th scale Wavestar model against the experimental data acquired during the test campaign. As in [6], the present validation study will follow an incremental procedure in which, first, wave-only cases will be validated, followed by wave excitation force, free decay, forced oscillation, and wave-induced motion cases. This allows an accurate assessment of potential misfits between experimental and numerical results.

Together with the validated model of a 1/5th scale Wavestar model presented by Windt et al. [6], the two validated numerical models will then form the basis of the analysis of the scaling effects of a point-absorber type WEC as pertinent future work.

1.3. Paper Outline

The remainder of the paper is organised as follows. Section 2 provides the necessary details on the physical wave tank at Aalborg University. The test cases, considered for model validation, are then introduced in Section 3. Section 4 details the setup of the numerical wave tank, including information on the governing equations, numerical wave generation and absorption method, as well as the domain layout. Then, results of the validation study are presented in Section 5, based on which conclusions are drawn in Section 6.

2. Physical Wave Tank

The experimental data, used within this validation study, were acquired during physical wave tank tests in the wave basin at Aalborg University. A schematic of the wave basin, including all relevant dimensions, is shown in Figure 1a. The tank measures 14.6 m in length and 13 m in width. Throughout the test campaign, free surface elevation data was measured with four resistive wave probes (WP1–WP4), whose locations are indicated in Figure 1a.

The Wavestar WEC consists of a hemispherical hull with a single operational DoF in pitch. In the full scale device, the hydraulic PTO system consists of a cylinder, pumping fluid through a generator, with a rated power of 500 kW for a device with 20 floaters [10]. Here, a 1/20th scale model of the full scale device is considered with an electrical, direct drive actuator PTO, inspired by the case study for the WECCOMP. In the wave basin, the device and the supporting structure are mounted on a gantry with a distance of 5.59 m to the wave maker paddles. Forces on the structure are measured with an S-type load cell, connecting the linear actuator with the arm and floating structure. The (translational) floater position is measured as the elongation of the linear actuator via an optical, laser position sensor.

A schematic and a photograph of the device are shown in Figure 1b,c, respectively. The structural properties are listed in Table 1. Note that the mass and inertial properties, as well as the location of the centre of mass are taken from [11] and were not explicitly measured during the test campaign.

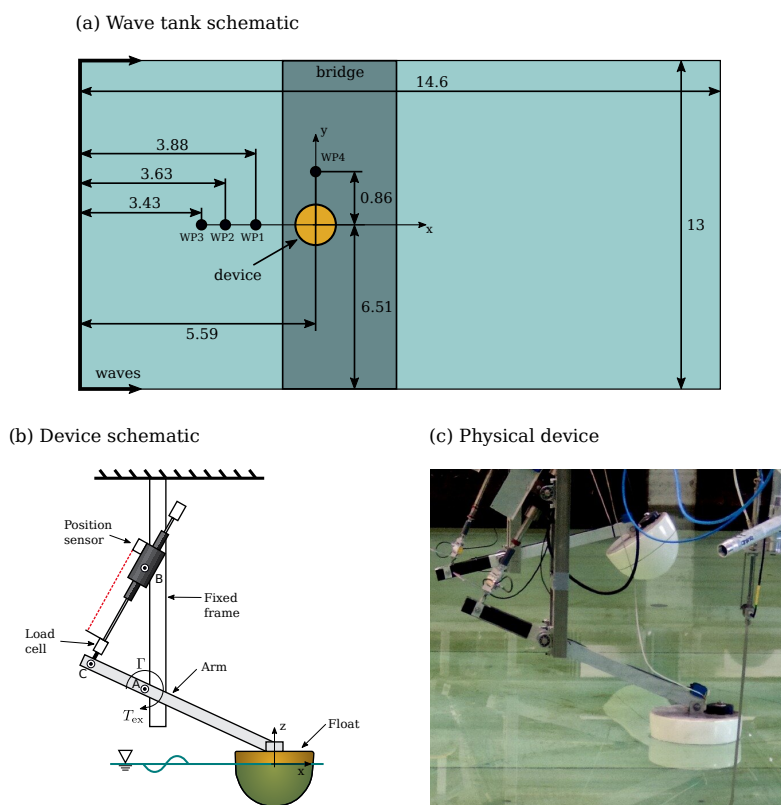


Figure 1. Schematic (not at scale) of the physical wave tank including the wave probe (WP) positions (all dimensions in [m]) (a) and the device (b). (c) shows a photograph of the physical device.

Table 1. Physical properties of the 1/20th scale Wavestar model. All measurements taken from [11] are printed in bold.

Hinge A:		
x	−0.449	m
y	0.000	m
z	0.232	m
Hinge B:		
x	−0.449	m
y	0.000	m
z	0.642	m
Hinge C:		
x	−0.636	m
y	0.000	m
z	0.303	m
Centre of Mass (CoM):		
x	−0.053	m
y	0.000	m
z	0.108	m
Mass (Float & Arm)	4.23	kg
Inertia (Float & Arm)	0.946	kg m ²
Floater diameter (at SWL)	0.256	m
Submergence (in equilibrium)	0.100	m
Water depth <i>d</i>	0.900	m

3. Test Cases

During the physical test campaign, a number of different test cases were considered including, amongst others, wave-induced motion of a controlled device [12]; however, for the validation of the CFD-based NWT, only the following five test cases, with incrementally increasing complexity, are considered.

Initially, to ensure an accurate representation of the incident waves in the numerical domain, wave-only test cases are considered (see Section 3.1). As highlighted in [13], an accurate representation of the free surface elevation is a key step for successful validation of a CFD-based NWT model against experimental wave tank data. To introduce wave-structure interaction, but still keep the complexity of the model relatively low, wave excitation force tests are considered (see Section 3.2). To get a preliminary understanding of the ability of the numerical model to capture the system dynamics, free decay tests are considered (see Section 3.3). Progressively increasing the complexity of the test cases, forced oscillation tests are studied (see Section 3.4), before considering wave-induced motion tests (see Section 3.5).

3.1. Waves-Only

For the wave-only test cases, the device is lifted out of the water and the waves are running through the tank undisturbed. The characteristics of the waves, i.e., wave ID, target wave height (The target wave height denotes the wave height specified within the wave maker controller.), H_{tar} , wave period, T , wave frequency, f , wave length, λ , and the wave steepness H_{tar}/λ , are listed in Table 2. During the wave-only tests, the free surface elevation is measured with four resistive wave probes, WP1-WP4 (see Figure 1), with a sampling rate of 1 kHz.

Table 2. Characteristics of the regular waves.

Wave ID	H_{tar}	T	f	λ	H_{tar}/λ
RW1	0.021 m	0.99 s	1.01 Hz	1.56 m	0.0135
RW2	0.063 m	1.41 s	0.71 Hz	2.93 m	0.0215
RW3	0.115 m	1.84 s	0.54 Hz	4.50 m	0.0256

3.2. Wave Excitation

During the wave excitation force tests, the WEC is locked in its equilibrium position, while being exposed to waves RW1–RW3. During these tests, the free surface elevation, as well as the wave excitation force are measured using resistive wave probes and the load cell (see Figure 1b), respectively.

3.3. Free Decay

For the free decay tests, the body is manually lifted out of its equilibrium position and then released to oscillate freely around the equilibrium position. Three consecutive experimental runs are considered. Translational position data of the WEC is recorded throughout the tests using the optical position sensor (see Figure 1b) and transformed into rotational displacement about joint A through geometric considerations.

3.4. Forced Oscillation

During the forced oscillation tests, the WEC is driven into motion by applying a defined input force through the linear actuator. Two different types of excitation can be distinguished, which are detailed in the following.

3.4.1. Single—Frequency Excitation

For the single—frequency excitation cases, a simple sinusoidal force signal is used to drive the system. Four different cases, with varying frequency and force amplitude, are considered. The excitation frequency correlates with the wave frequency ($1/T$) of waves RW1–RW3.

3.4.2. Multi—Frequency Excitation

The multi-frequency excitation experiments are initially performed for system identification purposes and are realised through up-chirp force signals [12,14,15]. The input force is defined as a linear frequency sweep in the range of $[0.7, 30]$ rad/s, with a fixed amplitude of 10 N. Note that, due to unavailability of the experimental force signal in the post-processing stage, the torque about the centre of rotation A is considered for the multi-frequency excitation experiments.

3.5. Wave-Induced WEC Motion

Finally, for the wave-Induced WEC motion tests, the (uncontrolled) WEC is exposed to the incident waves RW1–RW3 and the motion, as well as the free surface elevation are monitored.

4. Numerical Wave Tank

The CFD-based NWT is implemented using the open-source CFD toolbox OpenFOAM, version 4.1. The setup of the CFD-based NWT builds upon the validation study presented by [6], using the same solver settings and solution schemes, as well as similar boundary conditions. The problem discretisation is informed by the authors' previous work and adjusted to the considered wave characteristics. Only the numerical wave generation and absorption methodology (see Section 4.2) differ significantly from the numerical model presented in [6].

4.1. Governing Equations

In OpenFOAM, the incompressible Reynolds averaged Navier-Stokes (RANS) equations, describing the conservation of mass (Equation (1)) and momentum (Equation (2)), are solved using the finite volume method [16].

$$\nabla \cdot \mathbf{u} = 0 \quad (1)$$

$$\frac{\partial(\rho\mathbf{u})}{\partial t} + \nabla \cdot (\rho\mathbf{u}\mathbf{u}) = -\nabla p + \nabla \cdot (\nu\nabla\mathbf{u}) + \rho\mathbf{f}_b \quad (2)$$

In Equations (1) and (2), t denotes time, \mathbf{u} the fluid velocity, p the fluid pressure, ρ the fluid density, ν the kinematic viscosity, and \mathbf{f}_b external forces, such as gravity, per unit mass.

The pressure-velocity coupling is solved using the PIMPLE algorithm [17], blending the semi-implicit method for pressure-linked equations (SIMPLE) [18] and the pressure-implicit split-operator (PISO) [19].

To account for the two phase flow, the volume of fluid (VoF) method, proposed in [20], is used, following:

$$\frac{\partial \alpha}{\partial t} + \nabla \cdot (\mathbf{u}\alpha) + \nabla \cdot [\mathbf{u}_r\alpha(1 - \alpha)] = 0, \quad (3)$$

and

$$\Phi = \alpha\Phi_{\text{water}} + (1 - \alpha)\Phi_{\text{air}}, \quad (4)$$

where α denotes the volume fraction of water and Φ is a specific fluid quantity, such as density. \mathbf{u}_r is the compression velocity, determined as:

$$\mathbf{u}_r = \min [c_r|\mathbf{u}|, \max (|\mathbf{u}|)] , \quad (5)$$

where c_r is a user-defined factor to control the interface compression. Boundedness of the transport equation is achieved through the multi-dimensional limiter for explicit solutions (MULES) [21].

The body motion, induced by the incident wave or external force, is solved via Newton's 2nd law of motion, within the *sixDoFRigidBodyMotionSolver* in the OpenFOAM framework [22]. The motion solver provides a set of restraints, facilitating the numerical representation of the linear PTO. For the numerical forced oscillation tests, the experimentally measured excitation force (or torque) is fed to the numerical model through a modified restraint function in the motion solver. The successful use of the motion solver to replicate a linear actuator type PTO system is demonstrated in [6,23]. The resulting body motion is accommodated in the numerical domain through mesh morphing by means of the spherical linear interpolation (SLERP) algorithm.

Finally, regarding the flow conditions, turbulence is assumed to be a minor effect on the final results in this paper, based on [6,24], and laminar flow conditions are assumed for all simulations. It should also be noted that some studies in the WEC literature (e.g., [25,26]) highlight the complexity of turbulence modelling for WEC applications, in particular with respect to the correct wall treatment, by means of wall functions. The oscillatory nature of the flow around WECs makes it impossible to obey the well-known conditions on the y^+ value, requiring $30 < y^+ < 300$ for the accurate application of industry standard wall function, with a single grid over the course of the simulation. Thus, including turbulence modelling in the CFD-based NWT may, in fact, add inaccuracies and is, thus, omitted here.

4.2. Numerical Wave Generation and Absorption

Various methodologies are available in OpenFOAM to implement wave generation and absorption [27,28]. A static boundary method, proposed by Higuera et al. [29], for wave generation, together with a numerical beach, proposed by Schmitt and Elsässer [30], for wave absorption, is implemented in the present numerical model.

To ensure sufficient quality of the free surface elevation in [6], the relaxation zone method [31] is employed. It is well known that this methodology increases the computational overhead by introducing additional cells in the computational domain to accommodate the relaxation zones. In contrast, the static boundary method defines the relevant flow quantities, obtained from wave theory, as Dirichlet boundary conditions at the generation boundary of the CFD-based NWT. For the numerical beach, an additional dissipation term is introduced to the momentum equation of the Navier–Stokes equations, following:

$$\frac{\partial(\rho\mathbf{u})}{\partial t} + \nabla \cdot (\rho\mathbf{u}\mathbf{u}) = -\nabla p + \nabla \cdot (\nu\nabla\mathbf{u}) + \rho\mathbf{f}_b + \mathbf{S}\rho\mathbf{u}, \quad (6)$$

where \mathbf{S} controls the strength of the dissipation, equalling zero in the central regions of the domain where the desired wave field is required and then gradually increasing towards the boundary over the length of the numerical beach L_b . Here, Equation (7) is used to define the gradual increase of \mathbf{S} towards the domain boundaries.

$$\mathbf{S} = -2\mathbf{S}_{\max} \left(\frac{(L_b - x_b)}{L_b} \right)^3 + 3\mathbf{S}_{\max} \left(\frac{(L_b - x_b)}{L_b} \right)^2, \quad (7)$$

where x_b is the position within the numerical beach, equalling zero at the start and increasing to L_b at the NWT wall, and \mathbf{S}_{\max} denotes the maximum value of \mathbf{S} .

The combination of a static boundary method for wave generation [29], and a numerical beach for wave absorption [30], in this study can deliver good free surface elevation fidelity with minimal wave reflection and low cell counts. In fact, this is the first study employing this specific combination of the static boundary method and a numerical beach in OpenFOAM.

The optimal beach length, L_b , and the maximum damping factor within the numerical beach, \mathbf{S}_{\max} , are determined during preliminary simulations (see Appendix A) and are set to $1\lambda_{RW3}$ and 2.5 s^{-1} , respectively. A screen shot of the \mathbf{S} field is shown in Figure 2.

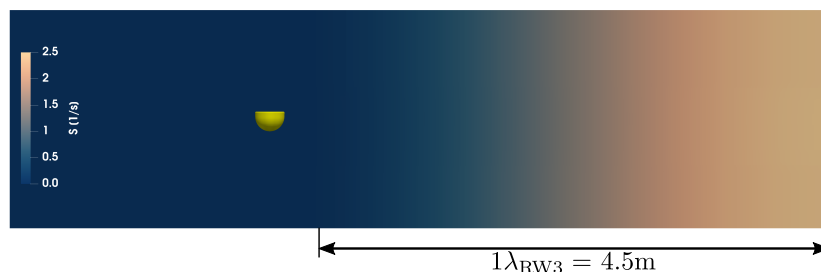


Figure 2. Side view of the computational domain: Screen shot of the \mathbf{S} field.

4.3. Computational Domain

The same computational domain is used for all the different test cases. Figure 3a,b show the side and top view of the numerical domain, including all relevant dimensions, respectively. To reduce the overall cell count, the symmetry of the problem is exploited and only half of the physical wave tank is modelled numerically. A symmetry boundary condition is employed in the xz -plane, where x points in the wave propagation direction, and z away from the tank floor (see Figure 3a). Furthermore, the width of the NWT is reduced and the distance between the wave generation boundary and the device location is shortened, compared to the physical wave tank.

The choice of the spatial and temporal discretisation sizes follows [6]. Spatially, the interface region in the simulation zone (see Figure 4) and region around the body are discretised with cells of a (vertical) size of 10 cells per wave height of $RW1$ (CPH_{RW1}) and a maximum aspect ratio of 4 in the horizontal and lateral direction, resulting in 186 cells per λ_{RW1} . The overall cell count is ~ 7.6 M cells. For the temporal discretisation, a fixed time step size of 0.001 s is used. For brevity, the individual

convergence studies are shown in Appendix B. A screen shot of the discretisation in the xz -plane is shown in Figure 4.

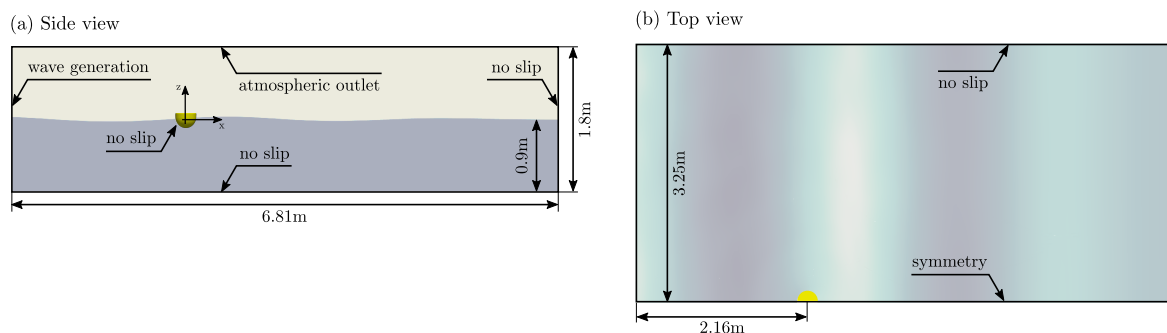


Figure 3. Schematic of the numerical wave tank: Side view (a) and top view (b).

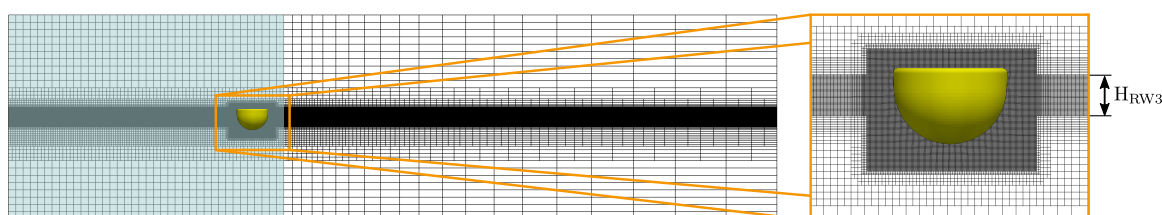


Figure 4. Screen shot of the computational mesh in the xz -plane. The simulation zone, in which the damping factor $S = 0$, is highlighted in blue.

5. Results and Discussion

This section presents the numerical results for the five different test cases introduced in Section 3, including a comparison with the experimental data.

5.1. Wave-Only

The long crested plane waves, considered in the present study, allow simulation in a two-dimensional domain, since such waves are invariant in the lateral direction.

Figure 5a–c show the phase averaged time traces of the free surface elevation, measured at wave probes WP1–WP4 (see Figure 1a), for waves RW1–RW3, respectively. The results of the (phase averaged) measured wave height, H , and the mean standard deviation, $\bar{\sigma}$, normalised by H , are listed in Table 3. The mean standard deviation $\bar{\sigma}$ is consistent between all wave probes and waves with values of the order of $\mathcal{O}(0.5\%)$, indicating relatively small deviation between consecutive wave periods, considered during the phase averaging.

As indicated in Figure 5a–c, more inconsistencies can be observed for the wave heights between the different wave probes. Specifically for wave RW3, significant discrepancies between the measured free surface elevation at wave probe WP1–WP3 ($H \approx 0.11$ m) and WP4 ($H = 0.095$ m) are found. Based on the increased spread between the wave probes, with increased wave height and period, it can be assumed that the observed behaviour stems from the influence of wave reflections due to the absorption capabilities of the physical wave tank.

The discrepancy between the different wave probes for the individual waves poses a challenge for the selection of the correct wave characteristic in the CFD-based NWT. Figures 6–8 show the comparison between the phase averaged experimental and numerical free surface elevation, measured at WP1–WP4, for waves RW1–RW3, respectively. For the individual waves, Table 4 lists the normalised root-mean square deviation (nRMSD), following:

$$\text{nRMSD} = \sqrt{\frac{\sum_{i=1}^n [y_{\text{exp}}(i) - y_{\text{num}}(i)]^2}{n}} \frac{100\%}{H_{\text{tar}}}, \tag{8}$$

where y_{exp} denotes the experimental quantity, y_{num} is the corresponding numerical quantity, and n defines the signal length via the number of samples. Normalisation is achieved by the target wave height H_{tar} , in Table 2.

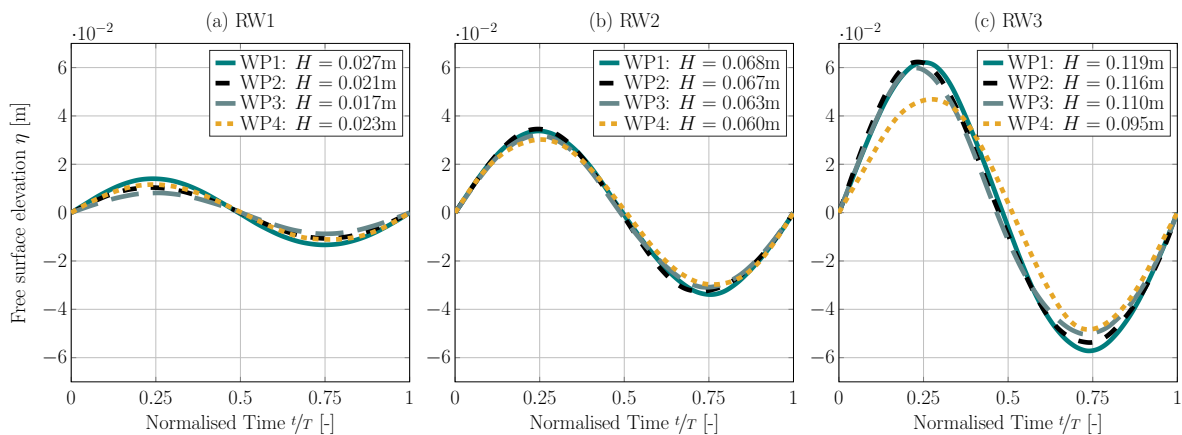


Figure 5. Phase-averaged free surface elevation, measured at wave probes WP1–WP4 (see Figure 1), for waves RW1 (a), RW2 (b), and RW3 (c).

Table 3. Wave height, H , and the mean standard deviation, $\bar{\sigma}$, normalised against the mean wave height, from the experimental data for waves RW1–RW3.

	RW1	WP1	WP2	WP3	WP4
H [m]		0.027	0.021	0.017	0.023
$\bar{\sigma}$ [%]		0.56	0.68	0.76	0.53
RW2					
H [m]		0.068	0.067	0.063	0.060
$\bar{\sigma}$ [%]		0.66	0.58	0.48	0.31
RW3					
H [m]		0.119	0.116	0.110	0.095
$\bar{\sigma}$ [%]		0.70	0.59	0.72	0.48

Table 4. nRMSD between the experimental and numerical free surface elevation, for waves RW1–RW3.

RW1	WP1	WP2	WP3	WP4
nRMSD [%]	8.31	3.86	10.70	2.27
RW2				
nRMSD [%]	4.66	4.78	2.82	2.42
RW3				
nRMSD [%]	2.87	3.75	5.00	9.26

Generally, a relatively good match in phase can be observed for all waves at all wave probes in Figures 6–8. Furthermore, Figures 6–8 reveal a consistent wave field within the CFD-based NWT for all waves, with negligible differences between the wave probes. The consistency in the wave field can be expected due to the excellent absorption capabilities achieved with the numerical beach, with reflection coefficient below 2% (see Appendix A). The difference in consistency of the experimental and numerical wave field leads to varying agreement between the experimental and numerical data (see Table 4), with a maximum deviation of 10.70% (RW1 at WP3). This varying agreement has to be taken into account for any further comparison between the experimental and numerical data.

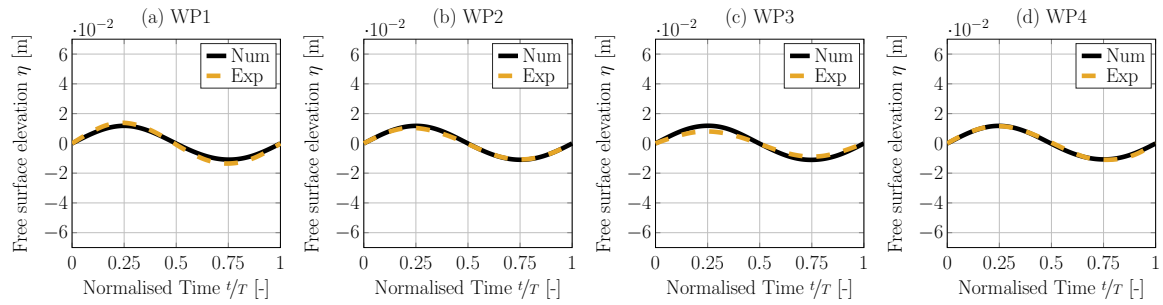


Figure 6. Phase-averaged free surface elevation, measured at wave probes WP1–WP4 (a–d), for wave RW1.

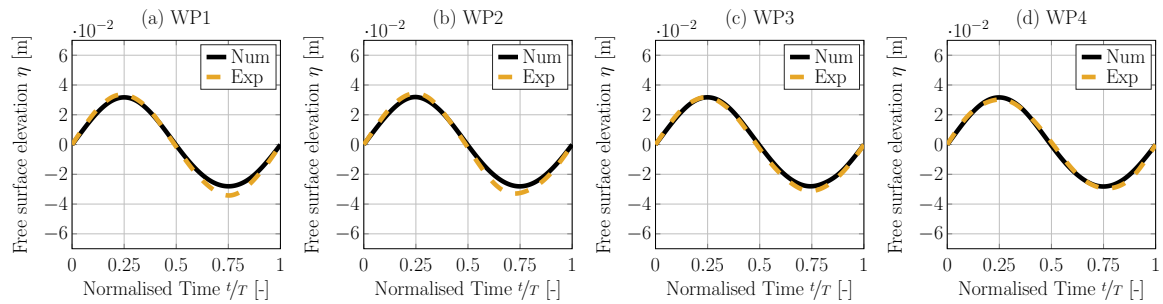


Figure 7. Phase-averaged free surface elevation, measured at wave probes WP1–WP4 (a–d), for wave RW2.

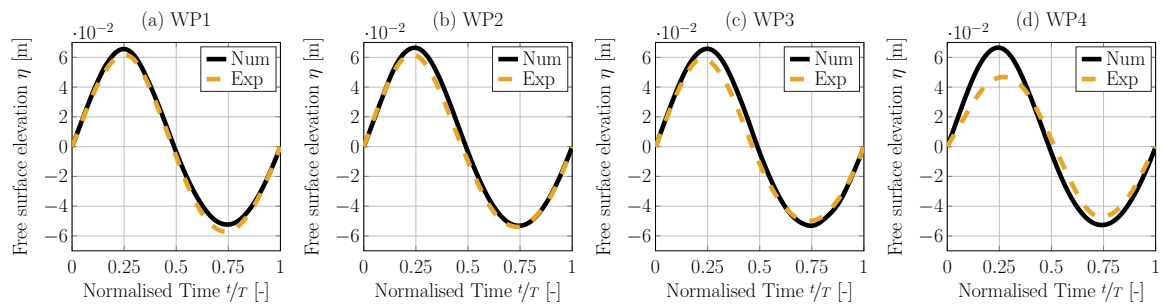


Figure 8. Phase-averaged free surface elevation, measured at wave probes WP1–WP4 (a–d), for wave RW3.

5.2. Wave Excitation

As stated in Section 3, the wave excitation force is measured with a load cell, connecting the linear actuator and the floater. From a post-processing point of view, it is simpler, in the CFD-based NWT, to extract the wave excitation torque, T_{ex} , instead of the linear force (see Figure 1b). Thus, from geometric considerations, T_{ex} is selected as the comparison variable in the following.

Figures 9–11 show the results of the phase averaged wave excitation torque T_{ex} , as well as the free surface elevation, measured at wave probes WP1–WP4. For a quantitative comparison, Table 5 lists the nRMSD between the experimental and numerical data. Note that the experimental excitation torque magnitude is used for the normalisation of the wave excitation torque RMSD.

For the free surface elevation, overall, similar agreement between the experimental and numerical data can be observed, compared to the wave-only cases. A notable deviation in the agreement between different wave probes for the individual waves is visible, showing an increased spread between the wave probes, with increased wave height and period, which is consistent with the wave-only cases and can likely be attributed to wave reflections from the tank wall in the physical experiments. Regarding the agreement between the experimental and numerical excitation torque, an expected close correlation between the agreement of the free surface elevation at WP4 (e.g., 3.04% for RW1

and 9.76% for RW3) and the agreement of T_{ex} (2.7% for RW1 and 12.48% for RW3) can be observed. Based on the observed correlation between the free surface elevation at WP4 and T_{ex} , together with the relatively large deviation between the numerical and experimental free surface elevation at WP4 for RW3 (see Figure 11d), an additional simulation has been run, reducing the numerical target wave height from the measured wave height of RW3 at WP1, i.e., 0.119 m, to the measured wave height at WP4, i.e., 0.095m (see Table 3). This case is henceforth referred to as RW3* and results are shown in Figure 12. As expected, the reduction of the numerical target wave height leads to relatively large deviations in the free surface elevation at WP1–WP3 (see Figure 12a–c); however reduces the nRMSD at WP4 from 9.76% for RW3 to 5.24% for RW3*. Furthermore, the acquired data follow the previously observed correlation between the agreement of the free surface elevation and the wave excitation torque, with a nRMSD of 5.24% at WP4 and 4.31% for T_{ex} .

Only the results for RW2 do not quite follow the observed correlation between the agreement of the free surface elevation and T_{ex} . A relatively small nRMSD of 1.93% for the surface elevation at WP4 is achieved, but a relatively large nRMSD of 9.32% is achieved for T_{ex} . The larger nRMSD for T_{ex} is induced by overall smaller T_{ex} amplitudes in the experimental data, compared to the numerical data. To rule out inconsistencies in the NWT, as a cause for the larger deviation, the wave field at a specific time instance is examined and screen shots of the dynamic pressure field are shown in Figure 13a–c, for waves RW1, RW2, and RW3*, respectively. For RW2, no apparent inconsistencies in the wave field are visible. At this stage, with the available data, no clear cause for the observed differences between the numerical and experimental T_{ex} data can be found.

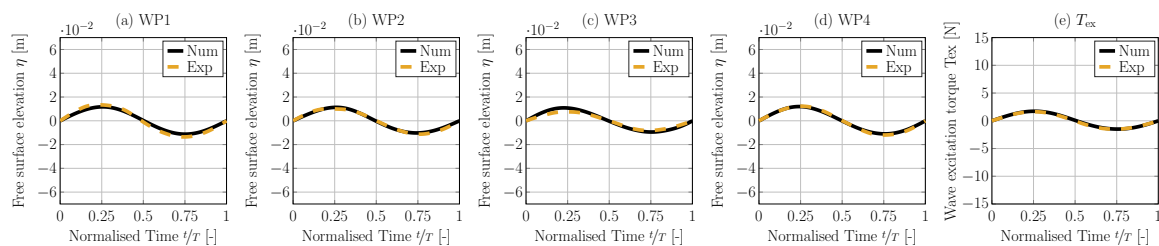


Figure 9. Phase-averaged free surface elevation, measured at wave probes WP1–WP4 (a–d), and wave excitation torque (e) for wave RW1.

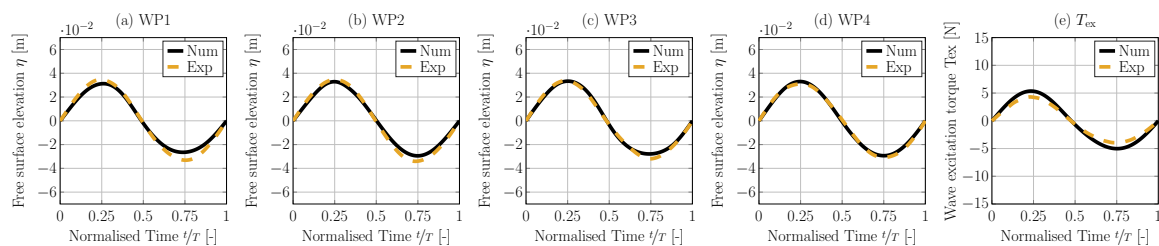


Figure 10. Phase-averaged free surface elevation, measured at wave probes WP1–WP4 (a–d), and wave excitation torque (e) for wave RW2.

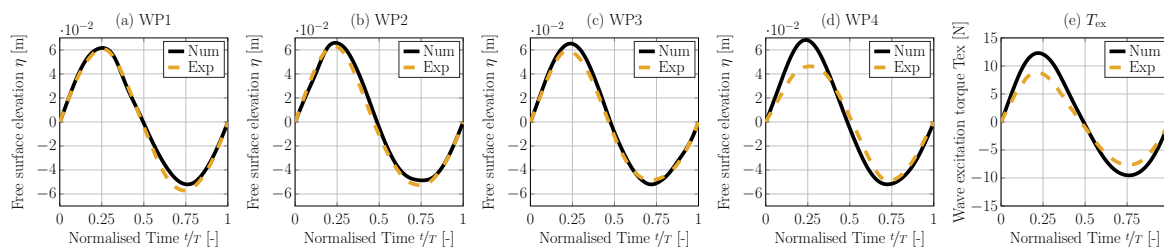


Figure 11. Phase-averaged free surface elevation, measured at wave probes WP1–WP4 (a–d), and wave excitation torque (e) for wave RW3.

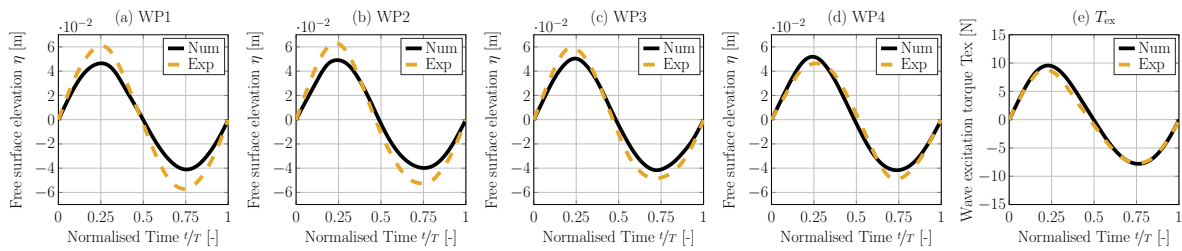


Figure 12. Phase-averaged free surface elevation, measured at wave probes WP1–WP4 (a–d), and wave excitation torque (e) for wave RW3*.

Table 5. nRMSD between the experimental and numerical free surface elevation and excitation torque for waves RW1–RW3.

RW1	WP1	WP2	WP3	WP4	T_{ex}
nRMSD [%]	8.49	3.83	8.42	3.04	2.70
RW2					
nRMSD [%]	5.56	4.45	2.82	1.93	9.32
RW3 ($H = 0.115$ m)					
nRMSD [%]	3.17	3.77	3.42	9.76	12.48
RW3* ($H = 0.095$ m)					
nRMSD [%]	12.14	10.97	7.70	5.34	4.31

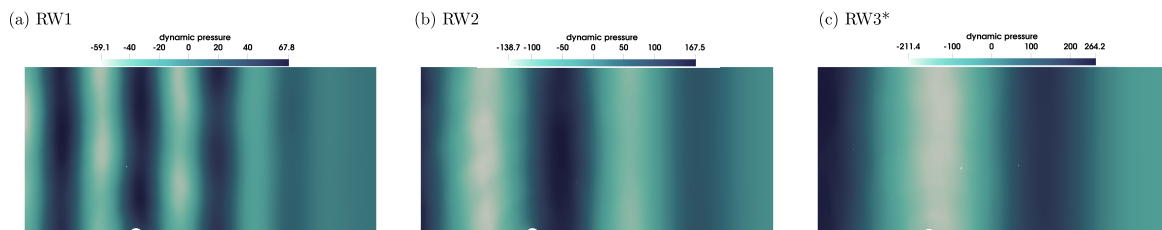


Figure 13. Screen shot of the dynamic pressure for waves RW1 (a), RW2 (b), and RW3* (c).

5.3. Free Decay

For the free decay test, experimental data from three different runs are available. Figure 14 shows the time trace of the normalised, rotational floater position, Γ , for the three different experimental runs and their mean value (see Figure 1b). From the experimental time trace, a natural period of ~ 0.8 s can be extracted for the WEC system. Figure 14 also includes time traces of the normalised floater position from numerical simulation. Specifically, results for four different values for the inertia of the system are plotted, i.e., 0.946, 0.600, 0.434, and 0.200 kg m². As stated in Section 2, initially, the inertia has been extracted from [11] and lumped using the parallel-axis theorem, resulting in 0.946 kg m². It can be seen, in Figure 14, that this value leads to an over-prediction of the amplitude as well as the period of the oscillation. Based on this result, two trial runs with a reduced inertia (0.3 and 0.2 kg m²) have been performed, resulting in an over- and under-prediction of the natural period of the system, respectively. Assuming, a quadratic relation between the value of the inertia and the natural period of the system, an inertia of 0.434 kg m² is estimated to deliver a natural period matching the experimental results, which can be confirmed from Figure 14. Note that the amplitude of the oscillation is still over-predicted in the numerical simulation; however, this is expected since no mechanical friction, likely to affect the experimental results [6], is modelled numerically. An inertia value of 0.434 kg m² is considered for all subsequent simulations.

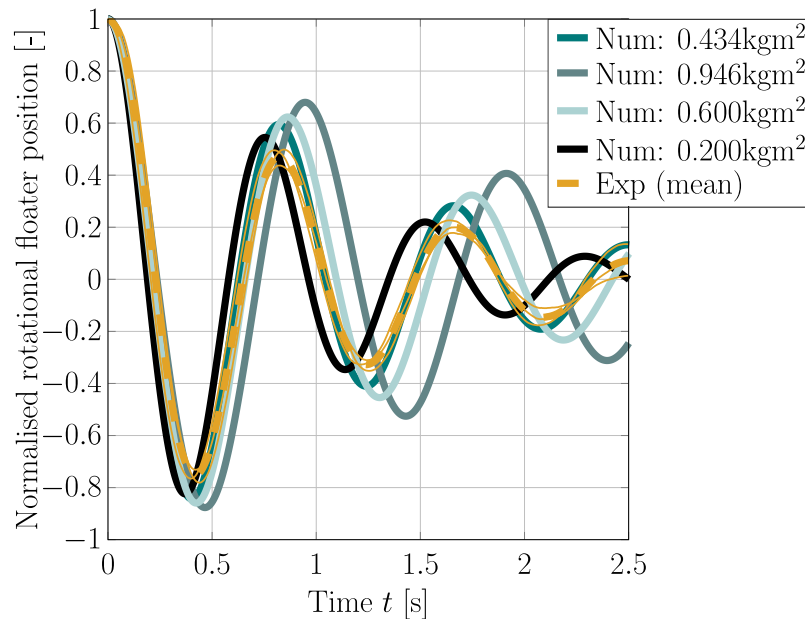


Figure 14. Time trace of the normalised floater position during the free decay test.

5.4. Forced Oscillation

As stated in Section 3, two different types of excitations are considered for the forced oscillation test: single- and multi-frequency excitation.

5.4.1. Single—Frequency Excitation

Figure 15a,b show the experimental and numerical time traces of the single-frequency (0.54 Hz) input force (5 N amplitude) and the resulting translational, floater position, respectively. It should be noted that, for the single-frequency cases, single-sided windowing is applied to the experimentally measured input force before feeding the force signal to the motion solver, to minimise the chance of numerical instability.

From Figure 15a, it can be seen that the force in the numerical simulation matches the experimental force after the initial windowing time. This is expected, since the measured experimental input force values are the input applied to the numerical simulation, and the time trace is included here merely as a cross check for the numerical setup. From the floater position data, plotted in Figure 15b, it can be seen that excellent agreement in phase is achieved between the experimental and numerical data. Relatively small difference in the motion amplitude can be observed at the peaks (e.g., $t = 11.5$ s) and troughs (e.g., $t = 18$ s). Consistent behaviour is found in Figure 16a,b as well as Figure 17a,b, showing time traces of the single-frequency excitation with a frequency of 0.54 Hz and 10 N force amplitude as well as with a frequency of 0.71 Hz and 5 N force amplitude, respectively. Again, excellent agreement between the experimental and numerical data is achieved in the phase of the floater position, while some differences can be observed at the peaks and troughs.

For both excitation force frequencies, it can be observed that, although a force signal with constant peak and trough amplitudes is applied during the experiments, the floater position shows visible inconsistency between consecutive peaks and troughs (e.g., between 11 and 14 s in Figure 17b). This behaviour is not visible in the numerical data. Analysing the measured free surface elevation (at wave probe WP4) for the experimental runs, negligible free surface perturbations can be measured (of the order of $\mathcal{O}(\leq 1 \cdot 10^{-3}\text{m})$), indicating that artefacts of the mechanical systems are the likely cause of the inconsistency in the experimental floater position signal. With the available experimental data, it is challenging to determine the exact cause of the observed behaviour.

Figure 18a,b show the experimental and numerical time traces of the single-frequency excitation force (with a frequency of 1.01 Hz and an amplitude of 5 N) and the resulting floater position,

respectively. It can readily be seen that the excitation close to the resonance frequency of the device (see Section 5.3) leads to considerably larger floater motion, compared to the excitation at 0.54 or 0.71 Hz. Consequently, the larger floater motion leads to larger free surface perturbation, potentially influencing the system through wave reflection within the physical wave tank. Potential wave reflection together with the artefacts of the mechanical system, suggested by the previous results, lead to relatively large differences between consecutive periods in the experimental data and, thus, to relatively large differences between the experimental and numerical results.

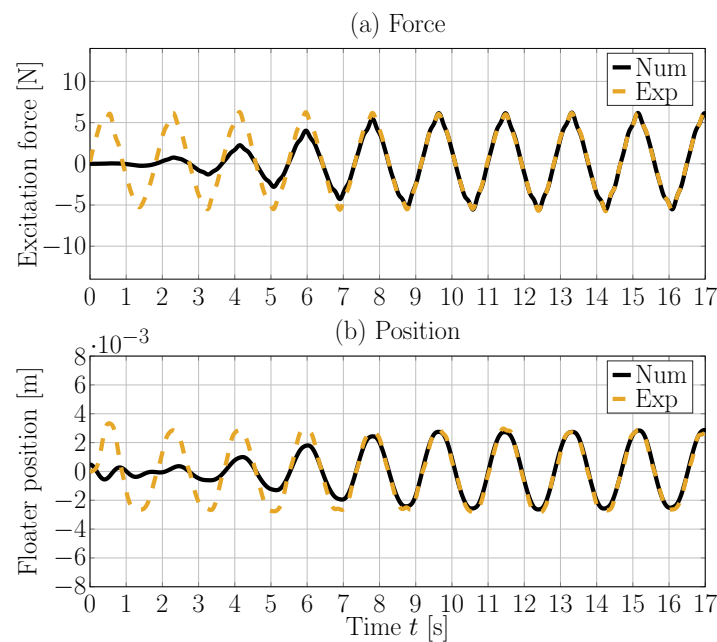


Figure 15. Time trace of the single-frequency (0.54 Hz) excitation force (a) and the floater position (b).

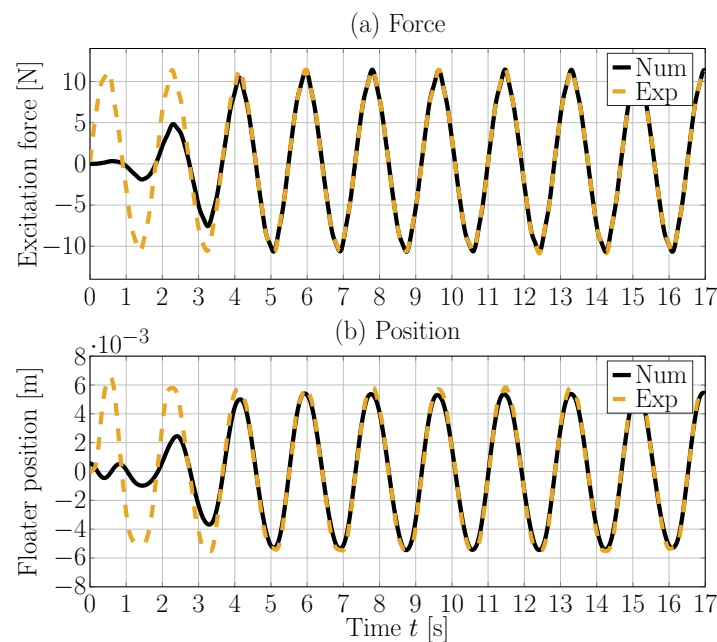


Figure 16. Time trace of the single-frequency (0.54 Hz) excitation force (a) and the floater position (b).

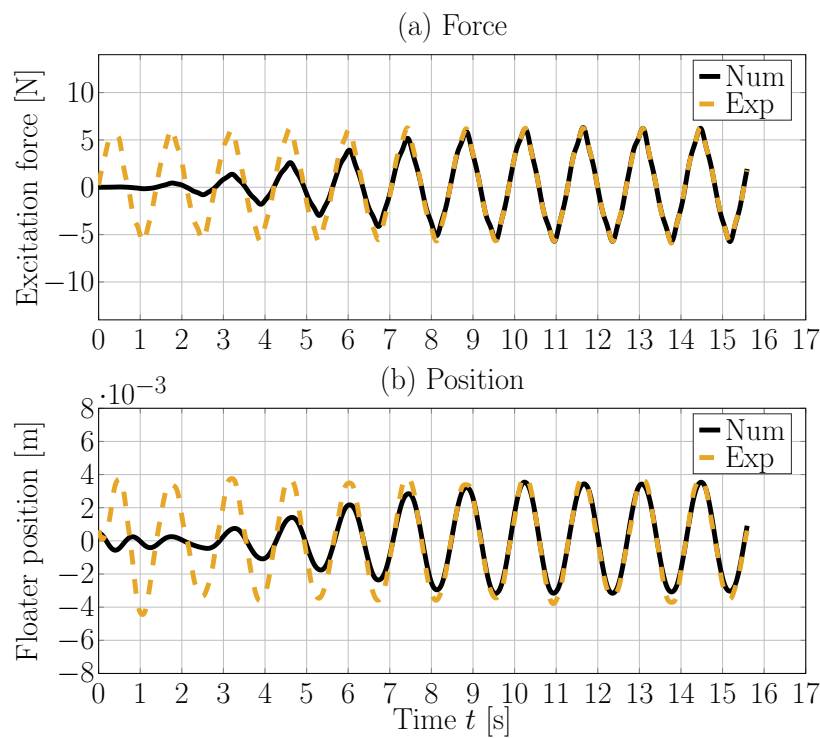


Figure 17. Time trace of the single-frequency (0.71 Hz) excitation force (a) and the floater position (b).

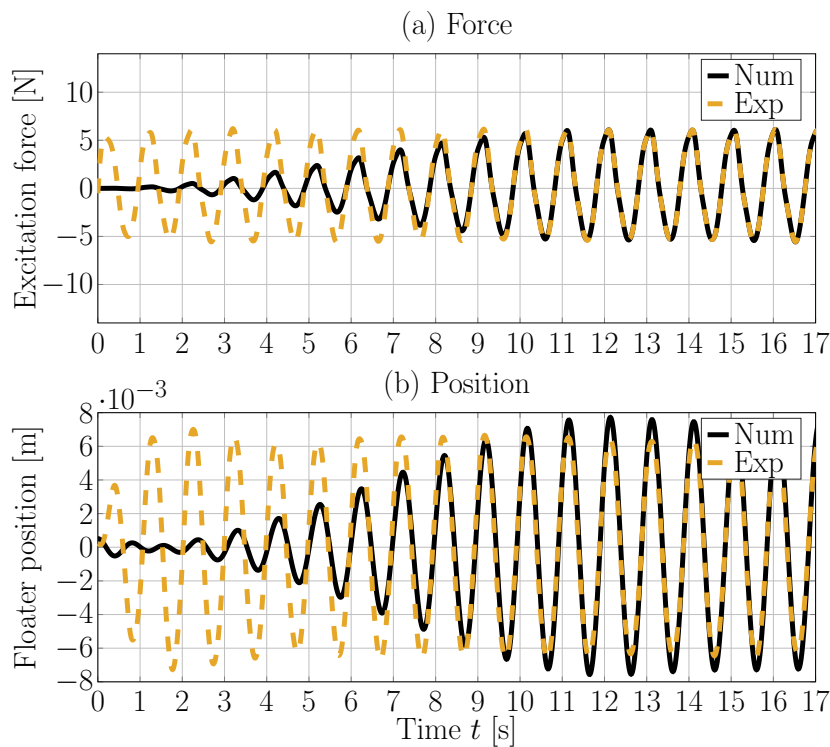


Figure 18. Time trace of the single-frequency (1.01 Hz) excitation force (a) and the floater position (b).

5.4.2. Multi-Frequency Excitation

The results for the multi-frequency excitation test case are plotted in Figure 19a,b, showing the excitation torque and the translational floater position, respectively. It should be noted that, in contrast to the single-frequency case, no single sided windowing is applied to the excitation torque, since the T_{ex} follows a relatively smooth trajectory. As shown in Figure 19a, the numerical and experimental

torque input virtually overlay each other. Comparing the experimental and numerical floater position data, a nRMSD of 6.3% can be computed. It is notable that the phase comparability shows a frequency dependency, manifesting itself as a mismatch in phase between $20 \text{ s} \leq t \leq 25 \text{ s}$. Similarly, a frequency dependency in the agreement between the amplitudes is visible, most notably between $20 \text{ s} \leq t \leq 22 \text{ s}$ and $24.5 \text{ s} \leq t \leq 27 \text{ s}$.

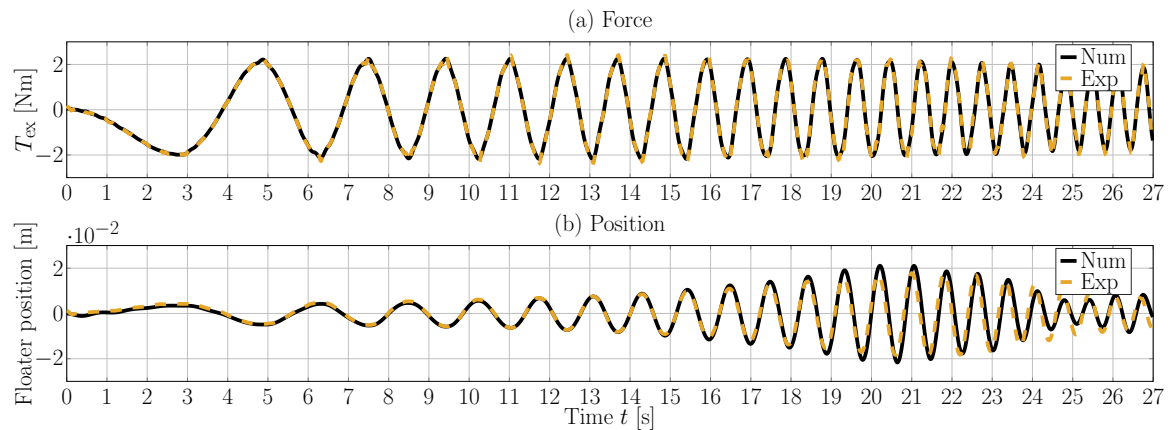


Figure 19. Time trace of the multi-frequency excitation torque (a) and the floater position (b).

Inspecting the free surface perturbation in the CFD-based NWT at $t = 25 \text{ s}$ (see Figure 20a), the differences between the numerical and experimental floater position between $24.5 \text{ s} \leq t \leq 27 \text{ s}$ can be attributed to the influence of reflected waves from the domain boundaries and the different reflection behaviour in the physical and numerical wave tanks. However, inspecting the free surface perturbation at $t = 21 \text{ s}$ (see Figure 20b) significantly smaller free surface perturbations can be observed in the CFD-based NWT. This suggests that the differences in the floater position amplitude between $20 \text{ s} \leq t \leq 22 \text{ s}$ may stem from mechanical features of the physical system, which are not captured in the CFD-based NWT.

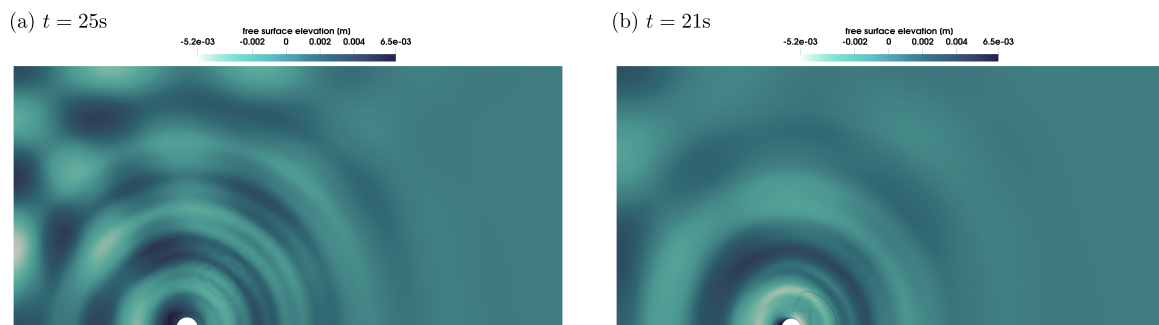


Figure 20. Screen shots of the free surface during the multi-frequency forced oscillation test at $t = 25 \text{ s}$ (a) $t = 21 \text{ s}$ (b).

5.5. Wave-Induced WEC Motion

Finally, cases of wave-induced WEC motion are considered for validation of the numerical 1/20th scale Wavestar model. Figures 21–23 show the phase averaged experimental and numerical free surface elevation at WP1–WP4, as well as the phase averaged floater position. The relevant values of the nRMSD are listed in Table 6. The target wave height H_{tar} and the experimental peak to trough magnitude of the floater position is used for normalisation of the RMSD for the free surface elevation and the floater position, respectively.

For wave RW1, excellent qualitative and quantitative (nRMSD = 0.32%) agreement for the floater position is found, with an nRMSD at wave probe WP4 of 2.56%. At wave probe WP4, waves RW3 and RW4 show similar nRMSD values; however, with nRMSD values of $\sim 5\%$ for the floater position.

A correlation between the agreement of the experimental and numerical data for the floater position and the free surface elevation at WP4 can be observed in Figures 22 and 23. It is notable that the numerical floater position at the peaks overestimates the experimental results for waves RW2 and RW3. Similarly, the peak in the free surface elevation is overestimated. At the troughs, the numerical floater position is overestimated; however, it is curious that an underestimation of the numerical free surface elevation troughs at wave probe WP4 can be observed. Overall, with maximum nRMSD values of 6%, the agreement between the experimental and numerical floater position data can be declared acceptable [2].

Table 6. nRMSD between the experimental and numerical free surface elevation and floater position for waves RW1–RW3*.

RW1	WP1	WP2	WP3	WP4	Floater Position
nRMSD [%]	8.91	4.42	10.99	2.56	0.32
RW2					
nRMSD [%]	4.45	4.56	3.73	2.28	6.06
RW3*					
nRMSD [%]	9.95	9.75	8.56	3.89	5.54

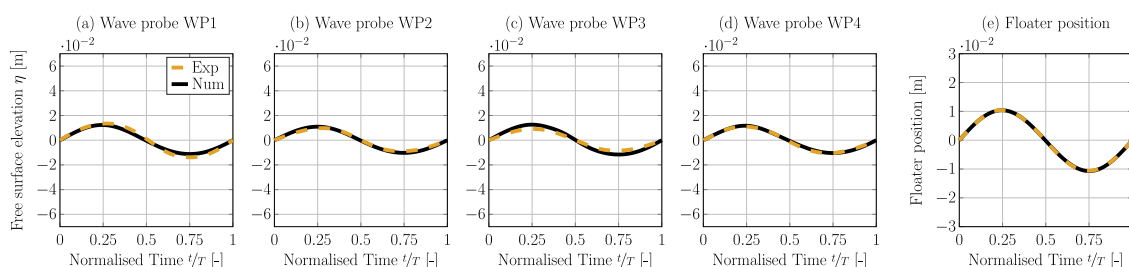


Figure 21. Phase-averaged free surface elevation, measured at wave probes WP1–WP4 (a–d), and floater position (e) for wave RW1.

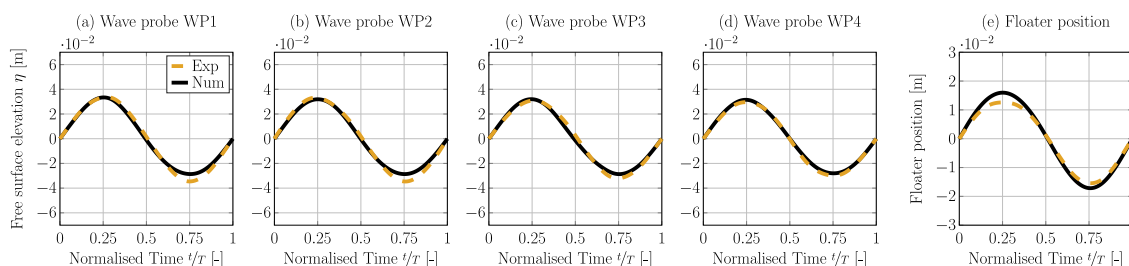


Figure 22. Phase-averaged free surface elevation, measured at wave probes WP1–WP4 (a–d), and floater position (e) for wave RW2.

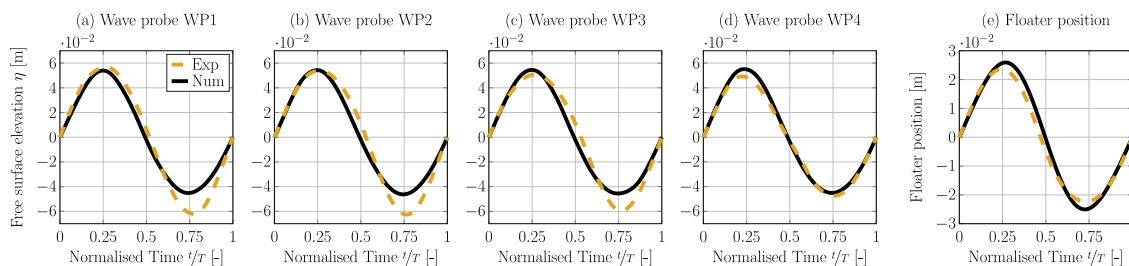


Figure 23. Phase-averaged free surface elevation, measured at wave probes WP1–WP4 (a–d), and floater position (e) for wave RW3*.

6. Conclusions

This paper documents the validation of a 1/20th scale numerical model of the Wavestar WEC against experimental data under various test conditions. From the results, the following conclusions can be drawn:

- The free surface elevation, measured in the physical wave tank, can be replicated numerically with acceptable agreement, considering the pollution of the physical data by wave reflection.
- The validation of a physical system requires exact knowledge of all system characteristics, especially difficult to measure quantities such as the moment of inertia, to avoid tuning of the numerical model, thereby undermining the confidence in the generality of the developed model.
- Considering the negligence of any mechanical friction in the CFD-based NWT model, the presented numerical model of the Wavestar WEC can be regarded as validated.

Author Contributions: Conceptualization, C.W., N.F., Y.P.-S., D.G.-V., J.D., F.F. and J.V.R.; methodology, C.W. and J.D.; software, C.W.; formal analysis, C.W., Y.P.-S. and D.G.-V.; investigation, C.W.; data curation, C.W., N.F., Y.P.-S., D.G.-V. and F.F.; writing—original draft preparation, C.W., N.F., Y.P.-S., D.G.-V., J.D., F.F. and J.V.R.; supervision, J.V.R.; project administration, J.R.; funding acquisition, J.R.. All authors have read and agreed to the published version of the manuscript.

Funding: The research leading to these results has received funding from the European Union Horizon 2020 Framework Programme (H2020) under grant agreement No. 731084. C. Windt, D. Garcia-Violini, Y. Peña-Sanchez, and N. Faedo are supported by the Science Foundation Ireland under Grant No. 13/IA/1886. J. Davidson is supported by the Higher Education Excellence Program of the Ministry of Human Capacities in the frame of Water science & Disaster Prevention research area of Budapest University of Technology and Economics (BME FIKP-VÍZ) and by the National Research, Development and Innovation Fund (TUDFO/51757/2019-ITM, Thematic Excellence Program).

Conflicts of Interest: The authors declare no conflict of interest.

Appendix A. Numerical Beach

To determine the optimal beach length, L_b , and maximum damping factor, S_{max} , a preliminary parametric study is performed. Generally, the numerical beach settings are dependent on the wave height and wave length [32], where longer wave lengths require longer beach lengths for efficient wave absorption. Thus, the longest (and largest) wave RW3 is used for the parametric study. Table A1 includes the reflection coefficient, R , determined based on the three point method in [33], for different combinations of L_b and S_{max} . Three wave probes with a spacing of $1/10\lambda_{RW3}$ and $1/4\lambda_{RW3}$ between the first and second and first and last wave probe, respectively, are employed, where the first wave probe is located at the intended device location.

Even with a beach length of $L_b = 1\lambda_{RW3}$ and a maximum damping factor of 2.5 s^{-1} , a reflection coefficient of 1.77% is achieved, which can be considered small [34]. No significant differences can be observed regarding the reflection coefficient for the different beach lengths with a maximum damping factor of 2.5 s^{-1} . Thus, to keep the overall cell count low, the shortest beach length is chosen for all subsequent simulations.

Table A1. Reflection coefficients for different combinations of L_b and D_{max} .

S_{max}	$L_{textb} = 1\lambda_{RW3}$	$L_b = 1.5\lambda_{RW3}$	$L_b = 2\lambda_{RW3}$
2.5 s^{-1}	1.77%	1.50%	1.68%
5 s^{-1}	3.50%	1.83%	1.74%

Appendix B. Convergence Studies

The same computational domain is used for all the different test cases. Thus, to determine the required spatial and temporal discretisation sizes, sea state RW1 (shortest wave period and smallest wave height) is chosen for the convergence study. Based on [28], three different cell and time step sizes

are tested, where the former is parametrised by the wave height, i.e., cells per wave height (CPH). The cell sizes (in the interface region) are: 5, 10, and 20CPH. The time step sizes are $\Delta t = 0.002$ s, 0.001 s, and 0.0005 s. The phase averaged wave height at the intended device location ($[x,y,z] = [0,0,0]$) is used as the input to the convergence study. The results of the (numerically) measured wave height, together with the convergence type and the discretisation uncertainty is listed in Table A2. For brevity, only temporal convergence studies are performed for RW2 and RW3, for which results are listed in Tables A3 and A4, respectively.

Table A2. Results of the spatial and temporal convergence study for RW1 ($T = 1$ s, $H = 0.02$ m).

Δz	Δt [s] 2×10^{-3}	Δt [s] 1×10^{-3}	Δt [s] 0.5×10^{-3}	Conv. Type	\bar{U}
5CPH _{RW1}	0.022	0.022	0.022	Monotone	0.7%
10CPH _{RW1}	0.022	0.023	0.023	Monotone	0.2%
20CPH _{RW1}	0.023	0.023	0.023	–	–
Conv. Type	Monotone	Monotone	Monotone		
\bar{U}	1.2%	0.3%	0.7%		

Table A3. Results of the temporal convergence study for RW2 ($T = 1.4$ s, $H = 0.060$ m).

Δz	Δt [s] 2×10^{-3}	Δt [s] 1×10^{-3}	Δt [s] 0.5×10^{-3}	Conv. Type	\bar{U}
5CPH _{RW1}	–	–	–	–	–
10CPH _{RW1}	0.059	0.061	0.061	Monotone	0.8%
20CPH _{RW1}	–	–	–	–	–
Conv. Type	–	–	–		
\bar{U}	–	–	–		

Table A4. Results of the temporal convergence study for RW3 ($T = 1.84$ s, $H = 0.094$ m).

Δz	Δt [s] 2×10^{-3}	Δt [s] 1×10^{-3}	Δt [s] 0.5×10^{-3}	Conv. Type	\bar{U}
5CPH _{RW1}	–	–	–	–	–
10CPH _{RW1}	0.099	0.100	0.100	Monotone	1.1%
20CPH _{RW1}	–	–	–	–	–
Conv. Type	–	–	–		
\bar{U}	–	–	–		

References

1. Roache, P.J. *Verification and Validation in Computational Science and Engineering*; Hermosa Publisher: Albuquerque, NM, USA, 1998; Volume 895.
2. Windt, C.; Davidson, J.; Ringwood, J.V. High-fidelity numerical modelling of ocean wave energy systems: A review of computational fluid dynamics-based numerical wave tanks. *Renew. Sustain. Energy Rev.* **2018**, *93*, 610–630.
3. Dai, S.; Day, S.; Yuan, Z.; Wang, H. Investigation on the hydrodynamic scaling effect of an OWC type wave energy device using experiment and CFD simulation. *Renew. Energy* **2019**, *142*, 184–194.
4. ITTC. *Recommended Procedures and Guidelines: Uncertainty Analysis Instrument Calibration (7.5-01-03-01)*; Technical Report; ITTC: Zurich, Switzerland, 2017.
5. Xu, Q.; Li, Y.; Yu, Y.H.; Ding, B.; Jiang, Z.; Lin, Z.; Cazzolato, B. Experimental and numerical investigations of a two-body floating-point absorber wave energy converter in regular waves. *J. Fluids Struct.* **2019**, *91*, 102613.
6. Windt, C.; Davidson, J.; Ransley, E.J.; Greaves, D.; Jakobsen, M.; Kramer, M.; Ringwood, J.V. Validation of a CFD-based numerical wave tank model for the power production assessment of the Wavestar ocean wave energy converter. *Renew. Energy* **2020**, *146*, 2499–2516.

7. Ransley, E.; Yan, S.; Brown, S.; Hann, M.; Graham, D.; Windt, C.; Schmitt, P.; Davidson, J.; Ringwood, J.; Musiedlak, P.H.; et al. A blind comparative study of focused wave interactions with floating structures (CCP-WSI Blind Test Series 3). *Int. J. Offshore Polar Eng.* **2020**, *30*, 1–10.
8. Ransley, E.; Brown, S.; Hann, M.; Greaves, D.; Windt, C.; Ringwood, J.; Davidson, J.; Schmitt, P.; Yan, S.; Wang, J.X.; et al. Focused wave interactions with floating structures: A blind comparative study. *Proceedings of the Institution of Civil Engineers—Engineering and Computational Mechanics*. Under review, 2020.
9. Ringwood, J.V.; Ferri, F.; Ruehl, K.; Yu, Y.H.; Coe, R.G.; Bacelli, G.; Weber, J.; Kramer, M.M. A competition for WEC control systems. In Proceedings of the 12th European Wave and Tidal Energy Conference (EWTEC) 2017, Cork, Ireland, 27 August–1 September 2017.
10. Hals, J.; Babarit, A.; Krokstad, J.; Muliawan, M.J.; Kurniawan, A.; Moan, T. *The NumWEC Project. Numerical Estimation of Energy Delivery from a Selection of Wave Energy Converters*; Technical Report; Norwegian University of Science and Technology: Trondheim, Norway, 2015.
11. Tom, N.; Ruehl, K.; Ferri, F. Numerical model development and validation for the WECOMP control competition. In Proceedings of the ASME 2018 37th International Conference on Ocean, Offshore and Arctic Engineering, Madrid, Spain, 17–22 June 2018; American Society of Mechanical Engineers Digital Collection: New York, NY, USA, 2018.
12. Garcia-Violini, D.; Peña Sanchez, Y.; Faedo, N.; Windt, C.; Ferri, F.; Ringwood, J. LTI energy-maximising control for the Wavestar wave energy converter: Identification, design, and implementation. *IEEE Trans. Control Syst. Technol.* **2020**, submitted.
13. Windt, C.; Davidson, J.; Schmitt, P.; Ringwood, J. Wave—Structure interaction of wave energy converters: A sensitivity analysis. *Proc. Inst. Civil Eng. Eng. Comput. Mech.* **2020**, in press.
14. Ringwood, J.; Davidson, J.; Giorgi, S. Identifying models using recorded data. In *Numerical Modelling of Wave Energy Converters*; Elsevier: Amsterdam, The Netherlands, 2016; pp. 123–147.
15. Davidson, J.; Giorgi, S.; Ringwood, J.V. Identification of wave energy device models from numerical wave tank data—Part 1: Numerical wave tank identification tests. *IEEE Trans. Sustain. Energy* **2016**, *7*, 1012–1019.
16. Weller, H.G.; Tabor, G.; Jasak, H.; Fureby, C. A tensorial approach to computational continuum mechanics using object-oriented techniques. *Comput. Phys.* **1998**, *12*, 620–631.
17. Holzmann, T. *Mathematics, Numerics, Derivations and OpenFOAM*; Holzmann CFD: Augsburg, Germany, 2016.
18. Patankar, S.; Spalding, D. A calculation procedure for heat, mass and momentum transfer in three-dimensional parabolic flows. *Int. J. Heat Mass Transf.* **1972**, *15*, 1787–1806.
19. Issa, R.I. Solution of the implicitly Discretised Fluid Flow Equation by Operator-Splitting. *J. Comput. Phys.* **1986**, *62*, 40–65.
20. Hirt, C.W.; Nichols, B.D. Volume of Fluid (VOF) Method for the Dynamics of Free Boundaries. *J. Comput. Phys.* **1981**, *39*, 201–225.
21. Henrik, R. Computational Fluid Dynamics of Dispersed Two-Phase Flows at High Phase Fractions. Ph.D. Thesis, Department of Mechanical Engineering, Imperial College London, London, UK, 2002.
22. Devolder, B.; Troch, P.; Rauwoens, P. Accelerated numerical simulations of a heaving floating body by coupling a motion solver with a two-phase fluid solver. *Comput. Math. Appl.* **2019**, *77*, 1605–1625.
23. Penalba, M.; Davidson, J.; Windt, C.; Ringwood, J.V. A high-fidelity wave-to-wire simulation platform for wave energy converters: Coupled numerical wave tank and power take-off models. *Appl. Energy* **2018**, *226*, 655–669.
24. Ransley, E.; Greaves, D.; Raby, A.; Simmonds, D.; Jakobsen, M.; Kramer, M. RANS-VOF modelling of the Wavestar point absorber. *Renew. Energy* **2017**, *109*, 49–65.
25. Schmitt, P.; Elsässer, B. The application of Froude scaling to model tests of Oscillating Wave Surge Converters. *Ocean Eng.* **2017**, *141*, 108–115.
26. Windt, C.; Davidson, J.; Schmitt, P.; Ringwood, J. Contribution to the CCP-WSI Blind Test Series 2: CFD-based numerical wave tank experiments employing an impulse source wave maker. In Proceedings of the 13th European Wave and Tidal Energy Conference, Naples, Italy, 1–6 September 2019; p. 1265.
27. Miquel, A.; Kamath, A.; Alagan Chella, M.; Archetti, R.; Bihs, H. Analysis of different methods for wave generation and absorption in a CFD-based numerical wave tank. *J. Mar. Sci. Eng.* **2018**, *6*, 73.
28. Windt, C.; Davidson, J.; Schmitt, P.; Ringwood, J.V. On the assessment of numerical wave makers for CFD simulations. *J. Mar. Sci. Eng.* **2019**, *7*, 47.

29. Higuera, P.; Lara, J.L.; Losada, I.J. Realistic wave generation and active wave absorption for Navier–Stokes models Application to OpenFOAM. *Coast. Eng.* **2013**, *71*, 102–118.
30. Schmitt, P.; Elsässer, B. A review of wave makers for 3D numerical simulations. In Proceedings of the MARINE 2015—Computational Methods in Marine Engineering VI, Rome, Italy, 15–17 June 2015; pp. 437–446.
31. Jacobsen, N.; Fuhrmann, D.R.; Fredsoe, J. A wave generation toolbox for the open-source CFD library: OpenFoam(R). *Int. J. Numer. Methods Fluids* **2012**, *70*, 1073–1088.
32. Schmitt, P.; Windt, C.; Davidson, J.; Ringwood, J.V.; Whittaker, T. The Efficient Application of an Impulse Source Wavemaker to CFD Simulations. *J. Mar. Sci. Eng.* **2019**, *7*, 71.
33. Mansard, E.; Funke, E. The Measurement of Incident and Reflected Spectra Using a Least Squares Method. In Proceedings of the International Conference on Coastal Engineering, Sydney, Sydney, Australia, 23–28 March 1980; pp. 154–172.
34. Cruz, J. *Ocean Wave Energy: Current Status and Future Perspectives*; Springer Science & Business Media: Boston, NY, USA, 2007.



© 2020 by the authors. Licensee MDPI, Basel, Switzerland. This article is an open access article distributed under the terms and conditions of the Creative Commons Attribution (CC BY) license (<http://creativecommons.org/licenses/by/4.0/>).